Journal of Materials Chemistry A

Accepted Manuscript

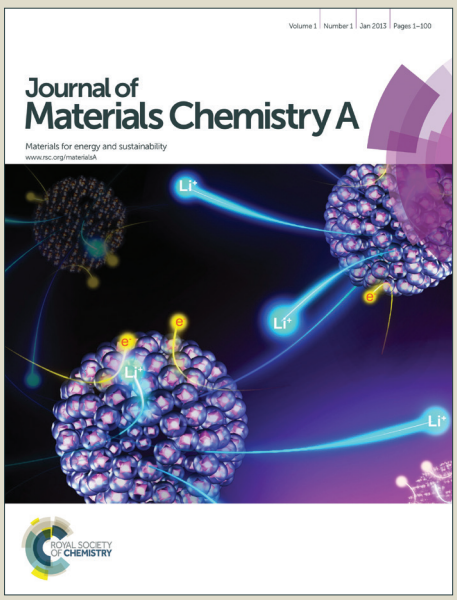

ROYAL SOCIETY OF CHEMISTRY

www.rsc.org/materialsA

Journal of Materials Chemistry A

RSCPublishing

ARTICLE

Influence of Different Chemical Modification to the Icephobic Properties of Superhydrophobic Surfaces under Condensate Environment

Yuanyi Wang,[a] Mingzhen Li,[a] Ting Lv,[a] Qingjun Wang,[a] Qingmin Chen*[a] and Jianfu Ding[b],

Cite this: DOI: 10.1039/x0xx00000x

Received 00th January 2014,
Accepted 00th January 2014

DOI: 10.1039/x0xx00000x

www.rsc.org/

Three superhydrophobic surfaces have been prepared on aluminum substrate, which was roughened by acid etching to form a nano-/micro-topological surface structure, and then the surface was modified by coating a PTES (a fluorinated coupling agent), TTPS (a siloxane coupling agent) or PA (an aliphatic coupling agent) layer. Their surface wettability in terms of water contact angle (CA), sliding angle (SA) and water droplet impact dynamics were studied under different humidity at -10 ℃. The reduction of ice adhesion was also investigated under both ambient and condensate environments. The results indicated that the icephobic properties of these three superhydrophobic surfaces at subzero environment varied wildly. The PTES surface can maintain an excellent sliding and rebounding ability of water droplet even under an extremely condensate condition (-10 ℃ and relative humidity (RH) 90%), while others cannot. It is worth to note that the ice adhesion obviously increased under a condensate environment, but no apparent ice-anchoring effect was observed on any of the three superhydrophobic surfaces. In addition, a water condensing dynamic study under subzero temperature revealed a distinctive Leidenfrost phenomenon-like jumping behavior of condensed droplets on all three superhydrophobic surfaces with the highest jumping scale and frequency on PTES surface. The excellent icephobic property of PTES surface indicates that the choice of a suitable chemical modification of superhydrophobic surfaces had significant influence on preserving water-repellency and icephobicity under extremely condensate conditions.

Introduction

Undesired ice accumulation on outdoor surfaces cause inconvenience for the daily life and also may result in severe issues and even loss of lives.[1-3] Although researches in this area have been carried out for decades,[4-6] environmentally harmless, economical, and efficient strategies for anti-icing remain to be developed. [7] Inspired by the anti-icing strategies of animals and plants in the nature, [8] superhydrophobic surfaces have received increasing attention in the development of icephobic materials.[9-11]

As stated in our previous work, an ideal icephobic surface should have the follow two characteristics. First, supercooled water droplets could roll off the surface rapidly before ice formation.[12-15] Second, the ice adhesion should be weak when ice accumulated on the surface.[16-18] Although the icephobic properties of some superhydrophobic surfaces were verified by experimental results,[10, 11] some other researchers still doubt about the practical application of superhydrophobic surfaces under condensate environment (low temperature and high humidity).[19-21] They claimed that the superhydrophobic surfaces would lose their entire hydrophobicity since the cavities on the rough surface could be wetted by the moisture from the environment upon freezing. Moreover, the condensed water in the cavities could turn to ice roots to anchor the ice layer into the rough surface structure so that the ice adhesion would increase with surface roughness.[22] Apart from experimental method diversity, sample difference is the primary cause for this controversy. They simply noticed the deterioration of superhydrophobicity but ignored that this anchoring effect can be prevented when the surface become hydrophobic enough to prohibit water entering the cavity through wetting process or even condensation.[23-27]

We have to admit that a overcooled condition would lead to a dramatic decrease in CA and a significant increase in SA [28] and a surface with a SA less than 10 ° in an overcooled or extremely condensing environment (-10 ℃, relative humidity (RH) 90%) hasn't been found in the literature among diversified superhydrophobic surfaces.[11, 29] However, the weakening extents of hydrophobicity were distinct to different

superhydrophobic surfaces. Some superhydrophobic surfaces turned into high viscosity at low temperature and high humidity condition [30] while others maintained the roll-ability of water droplet.[23, 31] In addition, further studies found that the growth status of condensed water droplets on the surface is the prime determinant to the wettability transition of a superhydrophobic surface. For example, Wier et al. [30] studied the condensation evolution on their micro-pillar array using an optical microscope, and observed that water droplets initially formed in the array voids, and then adjacent water droplets would consolidate, grow up and firmly anchor on the superhydrophobic surface in the end, causing the water droplet on the surface to lose mobility. On the contrary, Miljkovic et al. [24] demonstrated that when small droplets (≈10-100 μm) merge on a superhydrophobic surface, they undergo coalescence-induced droplet ejection or "jumping" independent of gravity due to the release of excess surface energy and the droplet accelerated and departs perpendicular off the surface. Such droplet jumping offers an avenue to maintain hydrophobicity of superhydrophobic surfaces under a condensate environment.[23] While a considerable amount of work has focused on understanding the effect of a specific morphological surface structure to sustain droplet jumping and water-repellency,[23-27] we believe that the contribution of surface chemical modification are also significant.[32-35]

In this work, three superhydrophobic surfaces with nearly uniform surface structure have been prepared by coating the roughened Al surface with three low surface energy coupling agents, PTES, TTPS and PA (see experimental for full name and structure). We explored the reason why some of them maintained roll-ability of droplet while others turned into high viscosity at low temperature and high humidity condition. This is the key challenge for active anti-ice/icephobic application of superhydrophobic surfaces. In this manuscript, both anti-ice/icephobic performances of different chemical modified superhydrophobic surfaces were revealed and proved by well-designed experiments (distinctive, simulated a condensate environment in which anti-ice/icephobic materials are more likely to applied). Besides, the dynamics of condensate water microdroplets were captured from microscopic to expose the essence behind varied anti-ice/icephobic performances: high-frequency bouncing of microdroplets is a necessary condition for maintaining active anti-ice/icephobic performance.

Experimental

Materials.

The aluminum plates (AA1060H24, 0.5 mm thick) were obtained from Southwest Aluminum (China). 1H,1H,2H,2H-perfluorodecyltriethoxysilane [$CF_3(CF_2)_7CH_2CH_2Si(OC_2H_5)_3$, PTES] and triethoxysilylethyl terminated polydimethylsiloxane [$(OC_2H_5)_3SiCH_2CH_2[(CH_3)_2SiO]_7CH_2CH_2Si(OC_2H_5)_3$, TTPS] were purchased from Fluorochem. Palmitic acid [$CH_3(CH_2)_{14}COOH$, PA] was supplied by Shanghai Lingfeng Chemical Reagent Co. Ltd (China). Diiodomethane was offered by Tokyo Chemical Industry Co. Ltd. The other chemicals including methanol, acetone, toluene, xylene, hydrofluoric acid (HF, 40 wt%) and hydrochloric acid (HCl, 37 wt%) were purchased from Nanjing Chemical Reagent Co. Ltd (China). All of them were used as received.

Sample preparation.

Surface etching: The as-received aluminum plates were rinsed ultrasonically with toluene, acetone and deionized water subsequently, and then dried at 23 ℃ for 24 h. The surface was then roughened by an acid etching process, which was done by soaking in a mixture of 2.5 mL of HF (40 wt%), 40 mL of HCl (37 wt%) and 12.5 mL of deionized water for 40 s，followed by thoroughly cleaning in an ultrasonic bath with deionized water to remove residual acids and drying in an oven at 100 ℃ for 2 h (Sample S40).

Surface modification: A PTES solution was prepared by dissolving PTES (0.5 wt%) in a mixture of methanol (88 wt%), deionized water (10 wt%) and HCl (0.1 M, 1.5 wt%). The other two (TTPS and PA) solutions were prepared by dissolving TTPS (0.5 wt%) in toluene and PA (0.5 wt%) in acetone, respectively. The surface modification of the aluminum plates with a smooth or roughened surface were done by coating with a PTES, TTPS or PA layer followed by a baking process for crosslinking. Therefore, the aluminum plate was dip-coated in the respective PTES or TTPS solution for four times and then cured at 100 ℃ for 6 h, or was dip-coated in the PA solution once and cured at 70 ℃ for 10 h.

Characterization.

Static contact angle (CA) and sliding angle (SA) were measured with a modified optical angle meter (Cam 200, KSV Instrument Ltd., Finland) in a microclimate chamber with a controlled humidity and temperature.[11, 28] The measurements were taken after 10 minutes of heat exchange and balance. Detailed humidity control and measurement method were illustrated in Figure S1 of supplementary information. The topographies and surface chemical compositions of roughened and coated samples were analyzed with an Ambios XI-100 surface profiler (Ambios Technology Corp., U.S.A) with a resolution of 0.2 nm, scanning electron microscopy (SEM, Hitachi S-4800, Japan) and a X-ray photoelectron spectroscopy (XPS, PHI5000 Versa Probe, ULVAC-PHI Inc., Japan) with monochromatic Al Ka radiation. Binding energies were calibrated by setting C1s line at 284.8 eV.

The impact experiments of supercooled water droplets were conducted using an apparatus reported in our previous work.[11] After the test samples were kept under target temperature and relative humidity for 10 minutes to get equilibrium, a high speed camera (Phantom v710, USA) was used to capture the overcooled droplets impact dynamics. Detailed experimental process and schematic diagram were shown in supplementary information and Figure S2. The ice adhesion tensile strength tests were performed using INSTRON 3366 universal testing machine (Instron Corp., USA) in an air-conditioned chamber

with a method described in our previous work.[11, 36]. Testing sample preparation was explained in supplementary information. The measurement model was also diagrammatized in Figure S3.

The water condensation process and in-situ tracking of condensed droplets self-combining behavior was both recorded with the help of a KYENCE VW-9000 high-speed microscope. In the test, the surfaces were cooled to -1 °C under an ambient environment (25 °C, RH 50~60% with a dew point about 13.9 ~ 16.7 °C). The initial 10 minutes of condensation was captured with a magnification of 500. The in-situ tracking of condensed droplets dynamic was captured with a magnification of 200 and a frame rate at 1000 frames per second (fps).

Results and discussion

A. Surface morphology and topography

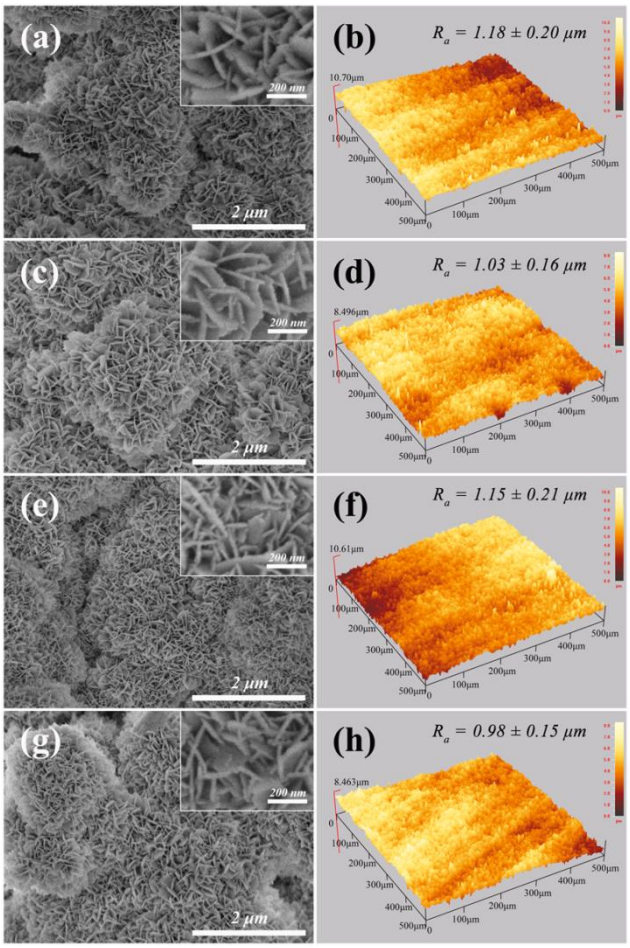

Figure 1. SEM images and three-dimensional surface profiles of the etched sample, S40 (a, b), and the PTES (c, d), PA (e, f) and TTPS (g, h) modified samples. The insets are SEM images with a higher magnification. Scale bars indicate 2 μm and 200 nm respectively.

The surface morphology and the three-dimension surface topography of the acid etched sample (S40) and three chemical modified rough samples were checked by SEM and surface profiler. In the surface topography tests, 8 random areas (500 μm× 500 μm) were scanned and average height (h) and roughness (Ra) of each sample was measured from these profiles with the result listed in Table S1.

The SEM images in Figure 1 showed that a binary nano-/micro-structure was formed by selective etching of vulnerable dislocation inside the Al crystals by the mixed acid solution.[37] The surface was fully covered with micro spheres which were densely assembled with nano-petals (S40, Figure 1a). No apparent change in the topography could be seen after the surfaces were modified with PTES, PA and TTPS (Figure 1c, e and g). The surface profiles in Figure 1b, d, f and h indicated that the average height (h) and roughness (R_a) of the four samples were almost consistent within a range of 5.10 ± 5% μm and 1.08 ± 10% μm, respectively. Therefore, we can reasonably consider that the sample coated with PTES, PA and TTPS have the same topological structure as the etched sample (S40).

B. Surface elemental analysis

Figure S4 displays the XPS spectra of S40 before and after the surface was modified with PTES, PA and TTPS with the atom abundance data listed in the inserted table. In this analysis, 5 random spots were tested on each sample and the reported data were the average of these five results. Due to the same substrate of the four samples, Al peaks (75.4 & 119.8 eV) and O element peak (531.6 eV) appeared on each spectrum. Besides, the peak of C element (284.5 eV) belonged to all three samples. In addition, the peak at high binding energy of 688.8 eV was attributed to F element in the PTES molecule. Similarly, the Si element peaks (100.9 & 152.0 eV) only appeared on the TTPS sample. This result indicated that the roughened Al surfaces have been successfully modified with PTES, PA and TTPS, respectively.

C. Surface free energy of the coatings

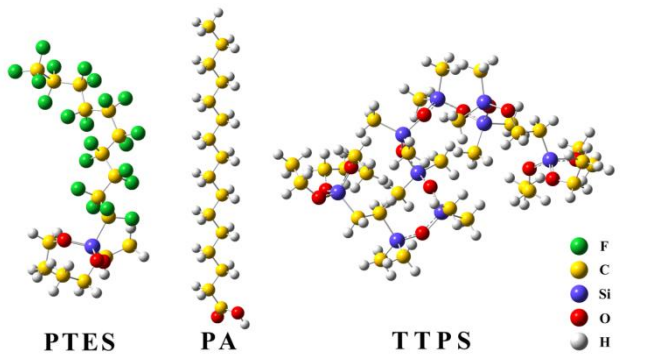

Figure 2. The geometries of PTES, PA and TTPS molecules optimized by theoretical calculations.

Theoretical calculations on the geometrical properties of PTES, PA and TTPS molecules were performed on the Gussian 09 program package. The geometries of these three molecules

were optimized with M06-2X,[38, 39] a density functional theory (DFT), using a basis set of 6-31g (d,p). As shown in Figure 2, the simulation revealed that PTES and PA intend to possess a rigid linear structure while TTPS had a curled molecular chain. The surface free energy of PTES, PA and TTPS coatings were determined with Owens-Wendt-Kaelble method.[40] After PTES, PA and TTPS were modified on flat aluminum surfaces, the water and diiodomethane contact angles were measured at 25 ℃. The results and calculated parameters [41] were listed in Table S2. Here, γ_L represented the liquid surface free energy which contained two parts, the dispersion force (γ_L^D) and the polarity force (γ_L^P) components. Accordingly, the solid surface free energy and its two respective components was γ_S, γ_S^D and γ_S^P. The results indicated that all these three surface coatings had a relatively low surface free energy (less than 30 mJ/m^2) which is necessary for a superhydrophobic surface. Compared to PA and TTPS, the fluorosilicone (PTES) surface had the lowest surface free energy at 13.4 mJ/m^2 owning to the compact and highly fluorinated side chain with the fluorocarbon bonds located on the surface.

D. Surface wettability

As shown in Figure 3, the water CA and SA measurements of PTES, PA and TTPS modified rough and smooth samples were taken under an ambient environment (25 ℃, RH=30%) and at -10 ℃ with different humidity (RH=30, 60, 90%). The solid–liquid contact area fraction (f) of the superhydrophobic surfaces was calculated on basis of their apparent CA (θ_{CB}) and the equilibrium CA of the corresponding smooth surfaces (θ) according to the Cassie-Baxter equation:[42]

$$f = \frac{\cos\theta_{CB}+1}{\cos\theta+1} \qquad (1)$$

At 25 ℃ and RH 30%, all the PTES, PA and TTPS coated surfaces possessed good superhydrophobic property with CA greater than 160 ° and SA smaller than 10 °. The PTES coated surface showed the highest superhydrophobicity both in static and dynamic measurements. This property could be of practical interest for anti-icing because deposited water droplets could be gravitationally removed from the subzero surfaces before freezing.[43] However, the condensed water may replace the air cushion, leading to a transition from the Cassie-Baxter state [42] to the Wenzel state [46] or their hybrid under condensate environment. Such transition has a close relation to the extent of supersaturation which is depend on temperature and humidity. Therefore, the wettability variation of a superhydrophobic surface under different humidity at low temperature could play a critical role to anti-icing performances.[14, 44, 45]

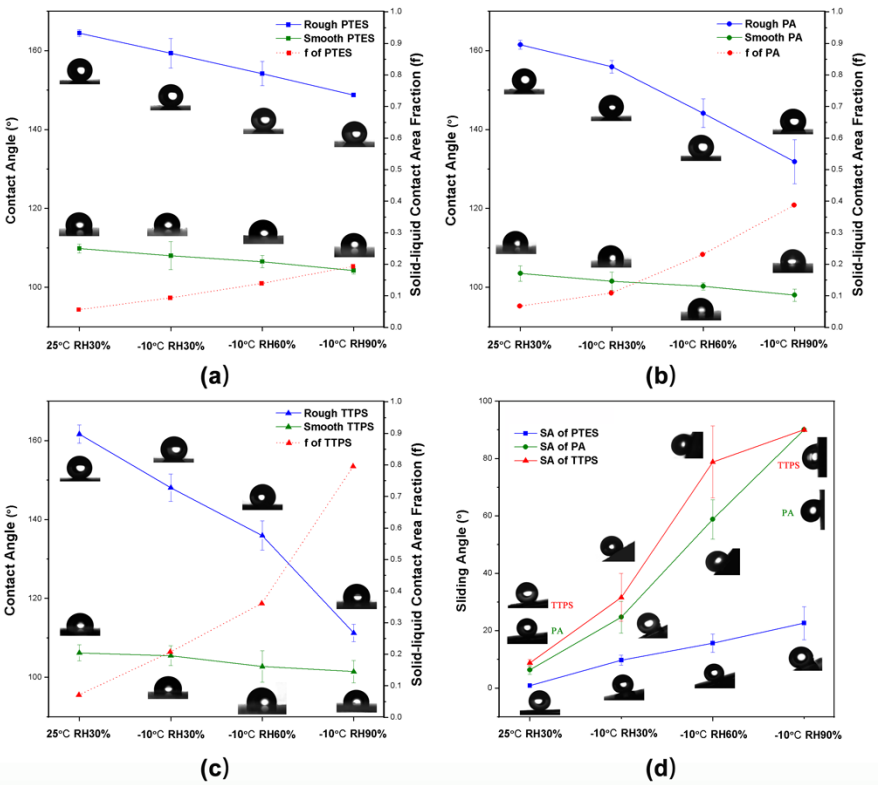

Figure 3. Water CA and solid-liquid contact area fraction according to the Cassie-Baxter equation at 25 °C with RH 30%, and at -10 °C with RH of 30, 60 and 90% on rough and smooth PTES surface (Figure 3a), PA surface (Figure 3b) and TTPS surface (Figure 3c). Water SA was also measured on three rough samples (Figure 3d) at the same temperature and relative humidity.

In the present work, the PTES demonstrated an excellent capability in maintaining the hydrophobicity under a highly condensing condition. When the temperature reduced from RT to -10 ℃ under 30% of RH, the CA of PTES surface slightly decreased from 164 ° to 159 °, and was further reduced to 154 ° and 152 ° with the RH increased to 60% and 90%. Meanwhile, its SA increased from 9.7 ° to 15.7 ° and 22.6 °, indicating the sliding ability survived on this surface even at the extreme condensate condition (RH of 90% at -10 ℃). This is similar to lotus leaf [47, 48] at the same condition (20 °).[49] However, the PA and TTPS displayed a quite different performance. When temperature reduced to -10 ℃, the SA of PA and TTPS surface dramatically increased from 6.3 ° and 8.7 ° to 24.7 ° and 31.6 ° even at a low oversaturation (RH = 30%).The sliding capability was further deteriorated with the saturation condition increased to RH 60%. In addition, water droplets hung upside down on the both surfaces under extreme condensing condition (-10 ℃, RH 90%). In this case, droplets would accumulate and then freeze on these surfaces which disabling the anti-icing capability eventually. Because of the same surface topography of these three samples, the varied wettability transition was mainly attributed to the chemical composition of the surface coatings. The experiment results suggested that the low free energy of the PTES surface (13.4 mJ/m^2) could lead to an excellent anti-icing performance.

E. Water droplet dynamic at subzero environment

When an overcooled water droplet was released to a solid surface, the kinetic energy of the droplet dissipated during the spreading process due to impacting, overcoming resistance from viscosity, converting to surface energy and so on. If the energy dissipation (mostly determined by the surface properties) during spreading was not too large, part of surface energy could revert to the kinetic energy and lead to retracting and rebounding.[44] Otherwise, the droplet remained pinned on the surface instead of fully withdraw and rebound before energy was expended. On the other hand, ice formation speed of an overcooled water droplet on solid surface depended on the growth rate of crystal nucleus. The ice formation of an overcooled water droplet on subzero surface could be delayed but could not be fully prevented. Mishchenko et al. [14, 50] showed that water droplets impinging on superhydrophobic surfaces exhibited a non-icing behavior if the time scale for droplet spreading and retracting from the surface was smaller than the ice nucleation time, and the droplet would bounce or roll off the surface before ice nucleating. In this case, the impacting water droplet could completely retract to a state similar to the static contact droplet in the Cassie-Baxter model after spreading and then elastically rebound before it froze. Therefore, it is possible to utilize this unique characteristic of superhydrophobic surface for anti-icing in subzero environments to remove water droplets timely to prevent water/ice accumulation [14, 50].

Figure 4 and Figure 5 displayed the impact behavior of overcooled water droplets (7.25 μL) on these three substrates at -10 °C from 50 mm height under a low (RH 50±5%) and a high humidity (RH 90±5%). Here, a small impact height (50 mm) was used in this test in order to reduce energy disturbing,[10] and thus the droplet impacted on the surface only in a low Weber number. A high-speed video camera was used to capture sequential images of the droplet at impact, contact, maximum spreading, maximum retraction, and rebound.[12] The respective diameters of the droplet at maximum spreading (d_{max}) and maximum retraction (d_{min}), and the rebounded height (h_{max}) were recorded. In the test, we define the time of each stage of an entire droplet impact cycle from impact to rebound as: t_1 (spreading time), the time from contact to maximum spreading with an average diameter of the contact area (d_{max}); t_2 (contracting time), the time from maximum spreading to complete contracting with an average diameter (d_{min}); and t_3 (rebounding time), the time from complete contracting to maximum rebounding with a height (hmax). Accordingly, the mean velocity for the droplet spreading, contracting and rebounding in these periods was v_1, v_2 and v_3 respectively, $v_1 = \frac{d_{max}}{t_1}$, $v_2 = \frac{d_{max} - d_{min}}{t_2}$, $v_3 = \frac{h_{max}}{t_3}$. The characterization data extracted from this test was summarized in Table 1.

Table 1. Dynamics data extracted from Figure 4 and Figure 5 for the impact on the superhydrophobic surfaces at relative humidity (RH) of 50±5% and 90±5% .

Sample	TA(°)	H(mm)	RH	d_{max}(mm)	d_{min}(mm)	h_{max}(mm)	v_1(m/s)	v_2(m/s)	v_3(m/s)
PTES	0	50	50±5%	4.17	0.00	9.46	1.73	0.60	0.24
PA	0	50	50±5%	4.25	0.00	8.09	1.88	0.53	0.25
TTPS	0	50	50±5%	4.27	0.00	7.99	1.79	0.49	0.23
PTES	0	50	90±5%	4.15	0.00	4.34	1.65	0.32	0.31
PA	0	50	90±5%	4.23	0.00	3.32	1.76	0.30	0.39
TTPS	0	50	90±5%	4.35	2.19	0.00	1.67	0.29	0.00

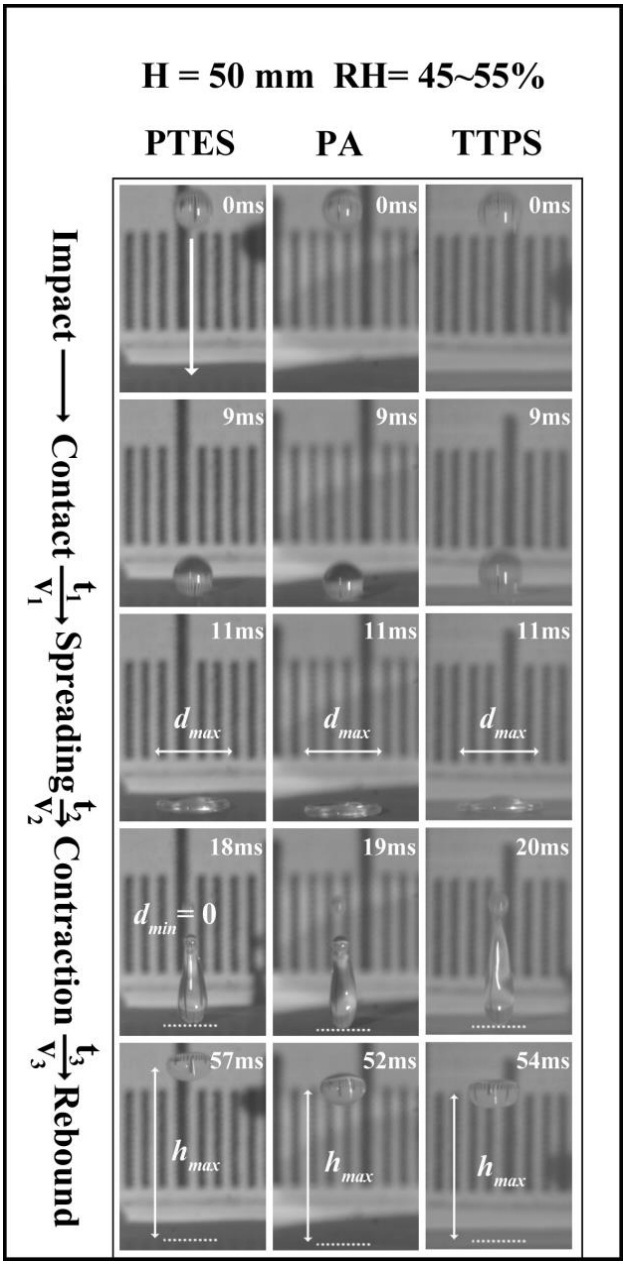

Figure 4. Sequential images of the dynamic behavior of a 7.25 μL supercooled water droplet impacting on three horizontal superhydrophobic surfaces from a height of 50 mm after the test samples were kept under target temperature and relative humidity for 10 minutes to get equilibrium at -10°C and RH of 50±5%: Images from top to bottom depict the droplet at impact, contact, maximum spreading (d_{max}), maximum retraction (d_{min}), and maximum rebound (h_{max}). The insert timestamps represent the relative time scale of the impact dynamic. Scale bars indicate 5 mm.

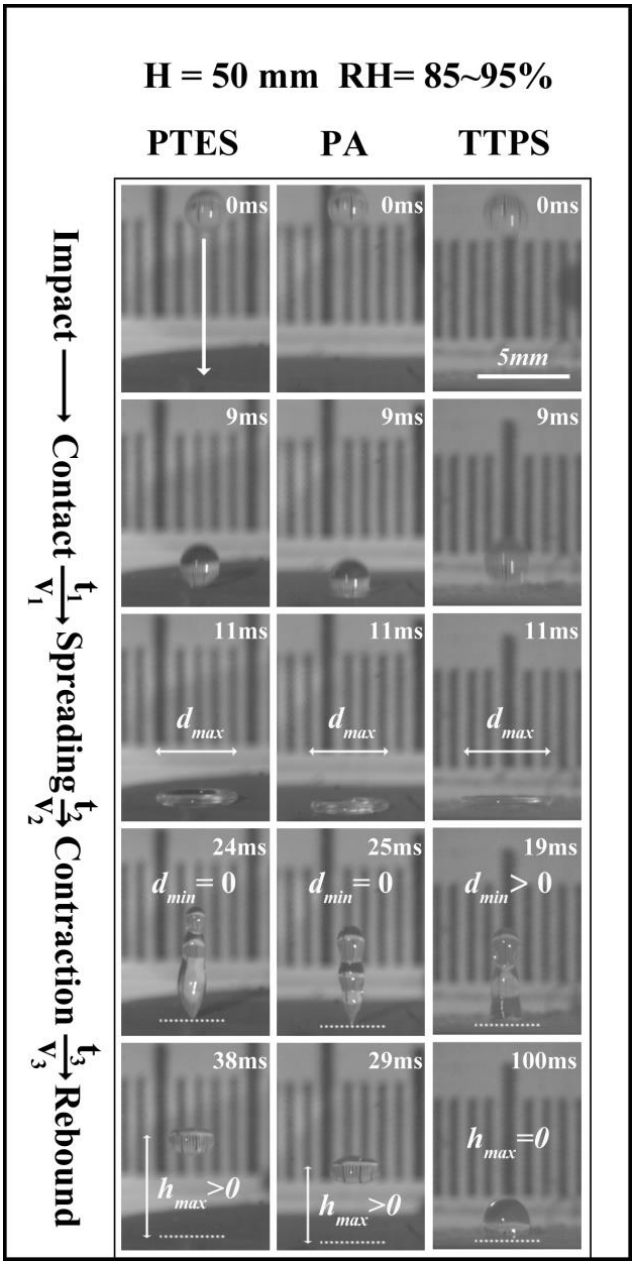

Figure 5. Sequential images of the dynamic behavior of 7.25 μL supercooled water droplet impacting on three horizontal superhydrophobic surfaces from a height of 50 mm after the test samples were kept under target temperature and relative humidity for 10 minutes to get equilibrium at -10°C and RH of 90±5%: Images from top to bottom depict the droplet at impact, contact, maximum spreading (d_{max}), maximum retraction (d_{min}), and maximum rebound (h_{max}). The insert timestamps represent the relative time scale of the impact dynamic. Scale bars indicate 5 mm.

Under low humidity of RH 50±5%, supercooled water droplet could rebound on all three superhydrophobic surfaces after a complete spreading and contracting process (Figure 4). The contracting time (t_2) was 18, 19 and 20 ms and the rebound height was 9.46, 8.09 and 7.99 mm on PTES, PA and TTPS surface, respectively. However, the contracting time was remarkably increased to 24, 25 and 19 ms accompanied by a dramatically decrease of rebounding height to 4.34, 3.32, and 0.00 mm when the relative humidity increased to 90±5% (Figure 5). During a droplet fell, its kinetic energy of droplet was only related to the releasing height, but not the surface properties. However, the kinetic energy and surface properties both contributed to the spreading for the droplet to reach d_{max}.[12, 45] This impact dynamics study indicated that kinetic energy loss dominated this process as d_{max} was almost the same on the hydrophilic, hydrophobic and superhydrophobic surfaces. The retraction process where the droplet diameter changed from d_{max} to d_{min} could mainly reflect the interaction between water

droplet and surface. In contracting period, v_2 decreased with the increase of humidity, suggesting that the droplet had a higher adhesion to the surface at high humidity. Moreover, the rebound height (h_{max}) remarkably dropped with the increase of humidity. The droplet couldn't even rebound on the TTPS surface under high relative humidity, indicating that the initial kinetic energy was not high enough to conquer the surface adhesion in this situation. In the practical application of icephobic materials under subzero environment, a shorter contact time and a higher rebounding height mean a more effective removal of impacting droplets and better performance of ice-repellent property. The most hydrophobic surface (PTES) kept the lowest water adhesion and thus a better ice-repellent performance can be expected. The v_3 data under high humidity showed a poor consistence. It is believed that this is caused by a large deviation in the rebounding height (h_{max}) measurement. Due to the high energy dissipation under the high humidity, the droplet rebound was incomplete to cause a large unsymmetrical deformation of the droplet. This could lead to a large deviation in the h_{max} measurement.[12]

F. Ice adhesion strength under condensate environment

From the above discussiones, it is clear that these three superhydrophobic surfaces could let overcooled water droplets rebound or roll off under a relative low humidity to serve as good icephobic surfaces.[14] However, under this highly condensing condition, water or ice would accumulate on the surface when the tilt angle is not big enough. Unfortunately, this type of weather was frequently encountered during heavy freezing rain and wet snow, where ice would eventually accumulated. In this case, the adhesion of the ice with the surface plays a critical role for an icephobic or anti-ice surface,[51] where the adhesion is expected to be as weak as possible. Comparing to other surfaces, superhydrophobic surfaces are possible to possess this ability when the air trapped beneath the water droplets can be maintained after freezing. It is claimed that in some cases the surface will be maintained at the Cassie-Baxter state and "Cassie ice or frost" could form on the surface with a reduced contact area,[9-11, 52] and thus the contact dependent adhesion between the formed ice and the substrate could be minimized. Some others asserted, under a high supersaturation condition, moisture and frost possibly accreted inside the micro-scale textures of the superhydrophobic surfaces, resulting in an ice layer penetrated into the textures to form a strongly interlocked "Wenzel ice", which could increase ice adhesion significantly.[19-22] These two judgments seem controversial on determining whether a superhydrophobic surface could reduce ice adhesion.

In view of this paradox, we studied the ice adhesion tensile strength on the three superhydrophobic surfaces both under an ambient and a high supersaturation condition. As demonstrated in Figure 7, the tensile ice adhesion strength increased from 1180 to 1500 KPa when the aluminum surface was roughened to form a binary nano-/micro-structure. It suggested that ice layer penetrated into the textures on the rough surface. Though the rough surface and superhydrophobic surfaces all have a similar surface texture structure, the ice adhesion strength on the superhydrophobic surface was significantly lower than that on the superhydrophilic surfaces. For example, the ice adhesion strength on the rough surface was about 10 times higher than that on the PTES superhydrophobic surface. Figure 7 also indicated that after the entire condensation process, the ice adhesion strength increased from 146 KPa, 314 KPa and 505 KPa to 292 KPa, 528 KPa and 1099 KPa on the superhydrophobic PTES, PA and TTPS surfaces, respectively. Fortunately, the highest ice adhesion strength on the condensed samples was still lower than those on flat aluminum and rough surface, suggesting that the icephobicity of superhydrophobic surface would be deteriorated under a high supersaturation situation but partially remain, i.e. limited ice-anchoring behavior was observed in the three superhydrophobic surfaces.

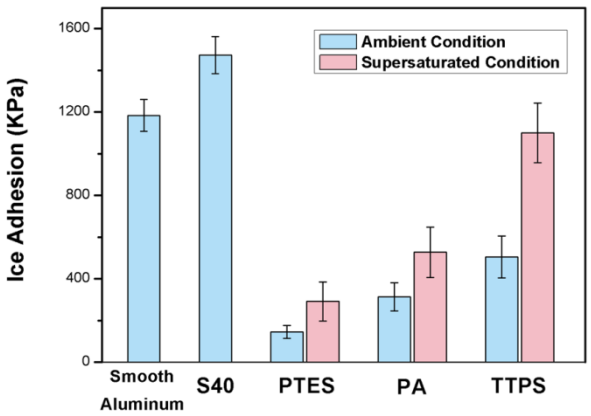

Figure 6. Tensile strength of ice adhesion on samples at −10 °C with sample assembly prepared at ambient condition (25°C and relative humidity about 50%) or supersaturated condition (-10 °C and relative humidity about 90%).

The impact dynamic test at -10 ℃ and the ice adhesion test both showed that the Cassie-Baxter state was at least partially remained on these three superhydrophobic surfaces under a supersaturated condition. In other words, the condensed water only occupied a fraction of the binary nano-/micro-superhydrophobic surface structure, which even lower on the PTES surface. This observation was verified by the solid-liquid contact area fraction (f) calculation, where a larger *f* value should be interpreted as a higher fraction of solid – liquid contact area, meaning more water condensates in the cavity of the structures. The results in Figure 3 indicates that the *f* value increased from 0.056 to 0.193 when the condensing condition changed from the ambient to the extreme supersaturated condition (-10 ℃ and RH 90%) on the PTES surface. This value increased to ~0.80 on the superhydrophobic TTPS surface. This result confirmed our observation in the above impacting and ice adhesion test, *i*.e., a superhydrophobic surface could partially maintain its Cassie-Baxter state even under a highly condensing weather condition.

G. Water condensing dynamics

Spontaneous removal of condensed water microdroplets from superhydrophobic surfaces is the key challenge for active anti-ice/icephobic application of superhydrophobic surfaces. Microdroplets could be removed from surfaces via self-propelled jumping induced by the coalescence of condensed microdroplets. This is achieved by converting the surface energy to the kinetic energy to overcome the gravity. [53] However, such self-propelled jumping of coalesced microdroplets cannot occur on some superhydrophobic surfaces at high supersaturation, because the condensed microdroplets tend to stay in the high adhesion Wenzel state which will affect the water-repellency directly. In this situation, it is a rational inference that the growth and distribution status of condensed microdroplets on superhydrophobic surfaces were contributed to be the inherent reason for different icephobic performances. Therefore, in order to explore the reason why some superhydrophobic surfaces maintained roll-ability of droplet while others turned into high viscosity at low temperature and high humidity condition, the water condensation process was studied (see Supplement video-1 for S40, video-2 for PTES, video-3 for PA and video-4 for TTPS).

The captured pictures at the moment of 0, 1, 2, 4, 6, 8 and 10 minutes of above mentioned videos were displayed in Figure 7. It shows that microdroplets formed on all three superhydrophobic surfaces in 60 s. At 60 s, PTES surface showed condensed droplets with a large size distribution, while PA and TTPS surfaces have droplets with a pretty narrow size distribution. The size distribution of the droplets on PTES surface increased remarkably at 120 s with the droplets relocated, indicating significant combining of the droplets due to their feasible movement on this surface. Between 120 to 600 second, no significant change was observed on the PTES surface regarding the droplet size and size distribution, seen as a constant frequency of the droplet relocation. However, on the PA and TTPS surfaces the droplets grew larger and stay almost motionless, indicating that a large number of droplets merged. On the other hand, no droplet formed on the superhydrophilic (S40) surface. The motion graph shown in Figure 7 gives an overview of the captured video. A higher volatility of the curve stands for a more frequent movement of the recorded images. This motion graph suggested the highest movement of the droplets on PTES surface regarding the scale and frequency, consistent with the conclusion from the above image analysis. This suggested that the efficiency of the self-propelled jumping on the superhydrophobic surfaces with same hierarchical structure can be tuned by changing the low surface energy chemical modification. Besides, an in-situ tracking self-combining behavior of the condensed droplets on PTES was carefully captured by side view. It showed that droplets jumped on the surface to land in the captured area and combined with other droplets on the surface and then jumped away (see Supplement video-5).

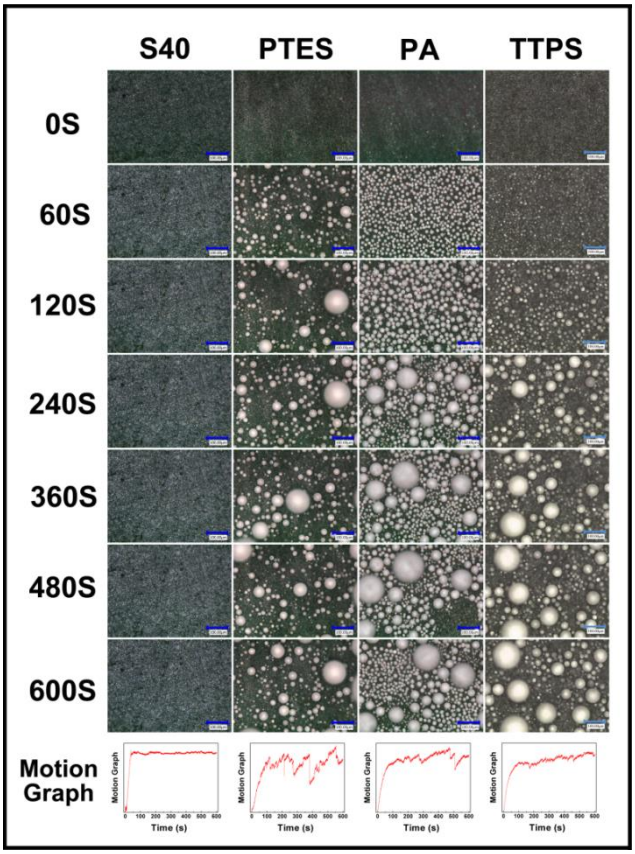

Figure 7. The initial 10 minutes of condensation dynamics on PTES, PA and TTPS surfaces at -1 °C under an ambient environment (25 °C, RH 50~60% with a dew point about 13.9 ~ 16.7 °C). Images from top to bottom depict the condensed microdroplets distribution at the moment of 0, 1, 2, 4, 6, 8, 10 minutes and motion graph of the dynamics. Scale bars indicate 100 μm.

More interestingly, the continuously jumping behavior could be seen macroscopically. We used a camera to capture this phenomenon after 4 minutes of condensation. As shown in Supplement video-6, water droplets splashed promptly on PTES surface like cold water fall into hot oil. However, the droplet jumping was only occasionally observed on PA and TTPS surface under the same condition (see Supplement video-7 and Supplement video-8). The jumping behavior on PTES surface after 1 minute, 5 minutes and 10 minutes was also recorded (see Supplement video-9, Supplement video-10 and Supplement video-11 respectively). At a longer condensing time, the number of condensed droplets slightly increased while the jumping frequency stayed at a relative high level. It can be speculated that the surface stays in the Cassie-Baxter state under this high supersaturation so that the condensed droplets can jump and move. This is believed to be the major cause of the outstanding ice-repellent and icephobic property of PTES surface.

Conclusions

Superhydrophobic surfaces have received increasing attention in the development of icephobic materials. In this paper, three

nano-/micro-aluminum surfaces with different chemical modification (PTES, PA and TTPS) were prepared by combining an etching and a coating process. At room temperature, all the surfaces possessed good superhydrophobic properties, with the PTES surface performing the best both in static and dynamic conditions. Under a highly condensate condition at subzero temperatures, these three superhydrophobic surfaces partially remained their hydrophobicity, and the PTES surface even maintained the sliding and rebounding behavior under an extreme condensate condition (-10 ℃ and RH 90%). This behavior leads to an excellent icephobic property, with ice adhesion strength on this surface only about 20% of the smooth aluminum surface. Besides, the dynamics of condensate water microdroplets were captured from microscopic to expose the essence behind varied anti-ice/icephobic performances. Distinctive self-combining and jumping behavior of condensed droplets was discovered on all three superhydrophobic surfaces. The PTES surface possesses the highest jumping scale and frequency which enables the surface to maintain its hydrophobic property under a condensate condition. It can be concluded that high-frequency bouncing of microdroplets on superhydrophobic surface is a necessary condition for maintaining active anti-ice/icephobic performance. This would help to make a better choice for anti-icing applications.

Acknowledgements

The authors would like to express thanks to Prof. Jun Xia and Mr. Jun Wu from Southeast University (Nanjing, China) for technical assistance with microscope observation measurement. This work is financially supported by a grant Nanjing University Testing Fund (No. 0205D100).

Notes and references

[a] Polymer Science and Engineering Department, School of Chemistry and Chemical Engineering, State Key Laboratory of Coordination Chemistry, Nanjing University, Nanjing, Jiangsu 210093, China

[b] Security and Disruptive Technologies, National Research Council Canada, Ottawa, Ontario K1A0R6, Canada

Electronic Supplementary Information (ESI) available: Supplement movies on the self-propel combining and jumping of condensed water droplets on different chemical modified superhydrophobic surfaces are available free of charge via the Internet at http://pubs.rsc.org. See DOI: 10.1039/b000000x/

1. J. Lu, Z. Jiang, H. Lei, H. Zhang, J. Peng, B. Li and Z. Fang, *Automation of Electric Power Systems*, 2008, **32**, 16-19.
2. N. Dalili, A. Edrisy and R. Carriveau, *Renew Sust Energ Rev*, 2009, **13**, 428-438.
3. A. K. Andersson and L. Chapman, *Accident Anal. & Prevention*, 2011, **43**, 284-289.
4. J. L. Laforte, M. A. Allaire and J. Laflamme, *Atmos Res*, 1998, **46**, 143-158.
5. D. Sanzo and S. J. Hecnar, *Environ Pollut*, 2006, **140**, 247-256.
6. O. Parent and A. Ilinca, *Cold Reg Sci Technol*, 2011, **65**, 88-96.
7. Q. F. Cheng, M. Z. Li, F. Yang, M. J. Liu, L. Li, S. T. Wang and L. Jiang, *Soft Matter*, 2012, **8**, 6740-6743.
8. J. F. Wang, Q. F. Cheng and Z. Y. Tang, *Chem Soc Rev*, 2012, **41**, 1111-1129.
9. J. B. Boreyko, B. R. Srijanto, D. N. Trung, C. Vega, M. Fuentes-Cabrera and C. P. Collier, *Langmuir*, 2013, **29**, 9516-9524.
10. A. Dotan, H. Dodiuk, C. Laforte and S. Kenig, *J Adhes Sci Technol*, 2009, **23**, 1907-1915.
11. Y. Y. Wang, J. Xue, Q. J. Wang, Q. M. Chen and J. F. Ding, *ACS Appl Mater & Inter*, 2013, **5**, 3370-3381.
12. D. Richard and D. Quere, *Europhys Lett*, 2000, **50**, 769-775.
13. P. Tourkine, M. Le Merrer and D. Quere, *Langmuir*, 2009, **25**, 7214-7216.
14. L. Mishchenko, B. Hatton, V. Bahadur, J. A. Taylor, T. Krupenkin and J. Aizenberg, *ACS Nano*, 2010, **4**, 7699-7707.
15. T. Maitra, M. K. Tiwari, C. Antonini, P. Schoch, S. Jung, P. Eberle and D. Poulikakos, *Nano Lett*, 2014, **14**, 172-182.
16. T. Ikeda-Fukazawa and K. Kawamura, *J Chem Phys*, 2004, **120**, 1395-1401.
17. S. Anand, A. T. Paxson, R. Dhiman, J. D. Smith and K. K. Varanasi, *ACS Nano*, 2012, **6**, 10122-10129.
18. P. Kim, T. Wong, J. Alvarenga, M. J. Kreder, W. E. Adorno-Martinez and J. Aizenberg, *ACS Nano*, 2012, **6**, 6569-6577.
19. S. Farhadi, M. Farzaneh and S. A. Kulinich, *Appl Surf Sci*, 2011, **257**, 6264-6269.
20. H. A. Stone, *ACS NANO*, 2012, **6**, 6536-6540.
21. J. Chen, J. Liu, M. He, K. Li, D. Cui, Q. Zhang, X. Zeng, Y. Zhang, J. Wang and Y. Song, *Appl Phys Lett*, 2012, **101**.
22. A. J. Meuler, G. H. McKinley and R. E. Cohen, *ACS Nano*, 2010, **4**, 7048-7052.
23. J. B. Boreyko and C. Chen, *Phys Rev Lett*, 2009, **103**.
24. N. Miljkovic, R. Enright, Y. Nam, K. Lopez, N. Dou, J. Sack and E. N. Wang, *Nano Lett*, 2013, **13**, 179-187.
25. C. Chen, Q. Cai, C. Tsai, C. Chen, G. Xiong, Y. Yu and Z. Ren, *Appl Phys Lett*, 2007, **90**.
26. J. Cheng, A. Vandadi and C. Chen, *Appl Phys Lett*, 2012, **101**.
27. X. Chen, J. Wu, R. Ma, M. Hua, N. Koratkar, S. Yao and Z. Wang, *Adv Funct Mater*, 2011, **21**, 4617-4623.
28. L. Yin, Y. Y. Wang, J. F. Ding, Q. J. Wang and Q. M. Chen, *Appl Surf Sci*, 2012, **258**, 4063-4068.
29. Q. Zhang, M. He, J. Chen, J. Wang, Y. Song and L. Jiang, *Chem Commun*, 2013, **49**, 4516-4518.
30. K. A. Wier and T. J. McCarthy, *Langmuir*, 2006, **22**, 2433-2436.
31. Y. T. Cheng and D. E. Rodak, *Appl Phys Lett*, 2005, **86**.
32. L. Cao, A. K. Jones, V. K. Sikka, J. Wu and D. Gao, *Langmuir*, 2009, **25**, 12444-12448.
33. R. Menini and M. Farzaneh, *Surf Coat Tech*, 2009, **203**, 1941-1946.
34. R. Jafari, R. Menini and M. Farzaneh, *Appl Surf Sci*, 2010, **257**, 1540-1543.
35. L. Zhu, J. Xue, Y. Wang, Q. Chen, J. Ding and Q. Wang, *ACS Appl Mater & Inter*, 2013, **5**, 4053-4062.
36. S. Yang, Q. Xia, L. Zhu, J. Xue, Q. Wang and Q. Chen, *Appl Surf Sci*, 2011, **257**, 4956-4962.
37. B. T. Qian and Z. Q. Shen, *Langmuir*, 2005, **21**, 9007-9009.
38. Y. Zhao and D. G. Truhlar, *AccChem Res*, 2008, **41**, 157-167.
39. Y. Zhao and D. G. Truhlar, *Theor Chem Acc*, 2008, **120**, 215-241.

40. F. M. FOWKES, *Ind and Eng Chem*, 1964, **56**, 40.
41. L. Cerne, B. Simoncic and M. Zeljko, *Appl Surf Sci*, 2008, **254**, 6467-6477.
42. A. Cassie and S. Baxter, *Transactions Faraday Soc*, 1944, **40**, 546-550.
43. X. Deng, L. Mammen, H. Butt and D. Vollmer, *Science*, 2012, **335**, 67-70.
44. A. Alizadeh, M. Yamada, R. Li, W. Shang, S. Otta, S. Zhong, L. Ge, A. Dhinojwala, K. R. Conway, V. Bahadur, A. J. Vinciquerra, B. Stephens and M. L. Blohm, *Langmuir*, 2012, **28**, 3180-3186.
45. L. Zheng, Z. Li, S. Bourdo, K. R. Khedir, M. P. Asar, C. C. Ryerson and A. S. Biris, *Langmuir*, 2011, **27**, 9936-9943.
46. R. N. Wenzel, *Ind and Eng Chem*, 1936, **28**, 988-994.
47. Q. F. Cheng, M. Z. Li, Y. M. Zheng, B. Su, S. T. Wang and L. Jiang, *Soft Matter*, 2011, **7**, 5948-5951.
48. M. X. Wu, H. Shuai, Q. F. Cheng and L. Jiang, *Angew Chem Int Edit*, 2014, **53**, 3358-3361.
49. L. Yin, Q. J. Wang, J. A. Xue, J. F. Ding and Q. M. Chen, *Chem Lett*, 2010, **39**, 816-817.
50. V. Bahadur, L. Mishchenko, B. Hatton, J. A. Taylor, J. Aizenberg and T. Krupenkin, *Langmuir*, 2011, **27**, 14143-14150.
51. S. A. Kulinich and M. Farzaneh, *Appl Surf Sci*, 2009, **255**, 8153-8157.
52. J. Lv, Y. Song, L. Jiang and J. Wang, *ACS Nano*, 2014, **8**, 3152-3169.
53. Q. Zhang, M. He, J. Chen, J. Wang, Y. Song and L. Jiang, *Chem Commun*, 2013, **49**, 4516-4518.

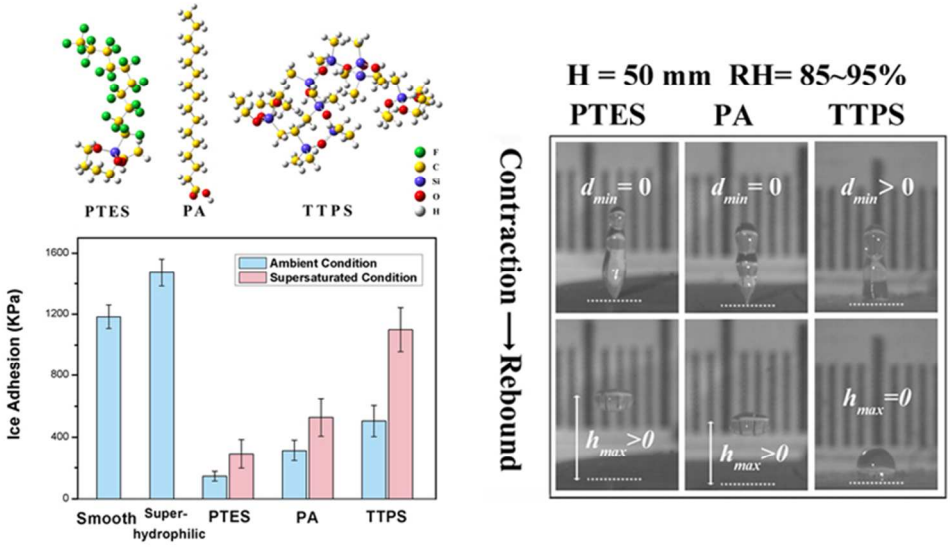

The icephobic properties (both in ice-adhesion reduction and water rebound) of different superhydrophobic surfaces varied wildly at subzero condensate environment.
71x39mm (300 x 300 DPI)